

Improving Composite Laminates Through Biomimicry

J.L. Liu, V.B.C. Tan,

J.L. Liu, National University of Singapore, e0011565@u.nus.edu

V.B.C. Tan, National University of Singapore, mpetanbc@nus.edu.sg

Keywords: Helicoidal configuration, composite plate, Finite elements, improvement through Biomimicry

Abstract

Previous research has shown that stacking unidirectional carbon fiber composite helicoidally with small angles can result in improvements in terms of maximum load resistance against transverse load. However explanations on why a helicoidal configuration has such performance have been lacking.

With the aim of identifying the main mechanism governing the load bearing capability of helicoidal laminates by compare them with common cross-ply configuration through simulations and experiments, we have found a relationship between unique damage pattern of helicoidal laminates and their strength. Under transverse loads, the specimens' stiffness will decrease when the fiber/matrix crack front propagating in the thickness direction merges with a large mid-plane delamination layer. Unlike cross-plys which suffer multiple delamination throughout the thickness, only a single large delamination initiate in single helicoidal laminates due to its stiffness pattern. This delays the large crack front that initiates at the bottom from reaching the delamination, which in turn delays drop in stiffness, and thus allows helicoidal structures to bear much higher transverse load.

Based on some preliminary findings on the failure of helicoidal laminates, some new laminate configurations are being tested with some already outperforming helicoidal laminates.

1 Introduction

Fiber-reinforced composites continue to attract the attention of industries with need for materials that are strong and light due to their high specific strength and stiffness. Materials like epoxy based carbon fiber composites are widely applied for their superior mechanical property. The demand for lighter and stronger materials never ceases. Instead of finding new materials with better properties, existing composite materials can also attain higher performance by altering their stacking orders.

Inspired by observations from the exoskeleton structure of crustaceans by Bouligand [1], several researchers have shown that stacking unidirectional carbon fiber composite helicoidally with small angles leads to improvement in terms of maximum load resistance in the transverse direction as shown by Shang, et al [2], Apichattrabrut and Ravi-Chandar [3], Cheng, et al, [4]. A 34% increase in peak load for 19-ply helicoidal laminates over cross-ply ones was reported by Shang, et al [2]. The study by Hong and Liu [5], Andersons and König, [6], Ravi-Chandar [7], Chen, et al, [8], Kim and Mayer, [16], Sebaey et la [17], Liu [18] looked into the effects of ply orientation on delamination. They showed that the difference in ply angle will result in different degree of delamination, which consequently affects the strength of the composite plate.

The damage mechanisms of helicoidal configuration are compared with a common cross-ply configuration in this study to determine the cause for the differences - what strengthens or weakens composite plates.

Hypothetical damage free stiffness vs displacement curves of different configurations were computed through computational simulations without considering damage to show which configuration has better stiffness if damage did not occur. Damage is then studied separately through many sets of simulations backed by experimental findings.

2 Experimental and simulation procedures

2.1 Materials and stacking sequence

Cross-ply and helicoidal laminates were fabricated from unidirectional T700/2510 carbon-epoxy prepregs (CU-075, CGT International, Singapore). Individual plies were cut into 100mm by 100mm squares and laid manually to the required configurations as described in Table 1. Specimens are then cured in an oven under 30 kPa pressures. The temperature is raised from room temperature to 140 °C over 2 hours and maintained for 2 hours. The specimens are then slowly cooled over 8 hours to room temperature. Five specimens were produced for each configuration. The mechanical properties of the material are summarized in Table 2.

Table 1. Laminate configurations

Designation	Description	Number of plies	Configuration
CP19	Cross-ply	19	[(0°/90°) ₉ /0°]
SH19	Single helicoidal	19	[0°/-10°/... /-180°]

Table 2. Mechanical and Physical properties of CU-075 prepreg (ASTM D790, ASTM D6641, ASTM D3518 Data acquired from Shang, et al [2] as specimens are made from the same material)

Property	Value
Nominal ply thickness	0.08mm
Areal density	0.121 kg/m ²
Modulus (fibre direction), E_1	107 GPa
Modulus (Transverse direction), E_2	7.99 GPa
In-plane shear modulus, G_{12}	4.00 GPa
Out-of-plane shear modulus, G_{23}	3.5 GPa
In-plane Poisson's ratio, ν_{12}	0.32
Out-of-plane Poisson's ratio, ν_{23}	0.45
Tensile strength (fibre direction), σ_{1t}	1650 MPa
Compressive strength (fibre direction), σ_{1c}	826 MPa
Tensile strength (transverse direction), σ_{2t}	45.1 MPa
Compressive strength (fibre direction), σ_{2c}	141 MPa
In-plane shear strength, τ_{12}	75.0 MPa

2.2 Transverse loading of specimens

Specimens were subjected to transverse point loads. The specimens are simply supported on one end of a circular cylinder with 75mm internal diameter allowing the specimen to flex under transverse loading

while providing out-of-plane constraint that is independent of in-plane orientation. A transverse point load is applied at the center of the specimen at a rate of 1 mm/min using a 12 mm diameter hemispherical indenter attached to a mechanical tester (AG-25TB, Shimadzu). The experimental setup is shown in *Figure 1*. Tested specimens were then viewed under a microscope to study the surface damage before they were cut by water jet to the required size and then sent for CT-scan. All CT scan images are side views taken from the center section of the plate as indicated in *Figure 2*.

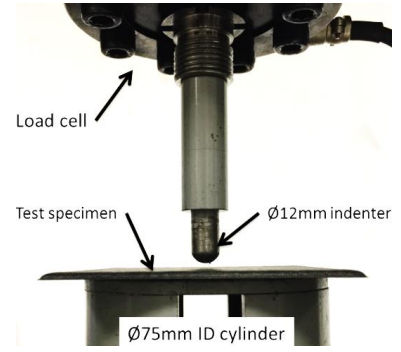


Figure 1. Experimental set up



Figure 2. SH19 sample before water jet machining (left), SH19 and CP19 sample after water jet machining (right)

2.3 Numerical Simulation of Damage Evolution

Numerical simulations were performed based on the parameters, model and methodology reported by Shang et. al. [2] to replicate the conditions of the experiments where the final damage predicted by the simulations was presented. Maximum stress criterion is incorporated for fiber-dominant failure, Tsai-Wu quadratic failure criterion [13] for matrix-dominated failure and mixed-mode decohesion elements for delamination [14]. Damage propagation in the simulation is handled through an energy based degradation model by Pinho et al [15].

Numerical simulations for SH19 and CP19 are performed using finite element software ABAQUS. The model is constructed with 19 layers of 100mm by 100mm by 0.08mm plies. Each ply consists of 8-node shell elements with reduced integration formulation (SC8R). Between every ply, a cohesive layer consisting of 8-node 3-D cohesive elements (COH3D8) is introduced to model interlaminar behavior. Damage of ply in the simulation represents matrix or fiber damage, damage in the cohesive layers represents delamination. Both ply and cohesive layers have similar mesh and the mesh is refined within a 20mm by 20mm area at the center of the laminate. The indenter is modeled as a 12mm rigid hemisphere.

Table 3. Input parameters for simulation

Property	Value	Remarks
Modulus (fiber direction), E_1	107 GPa	ASTM D3039
Modulus (Transverse direction), E_2	7.99 GPa	ASTM D3039
In-plane shear modulus, G_{12}	4.00 GPa	Tomblin [9]
In-plane Poisson's ratio, ν_{12}	0.32	ASTM D3039
Tensile strength (fiber direction), σ_{1t}	1650 MPa	ASTM D3039
Compressive strength (fiber direction), σ_{1c}	826 MPa	ASTM D6641
Tensile strength (transverse direction), σ_{2t}	45.1 MPa	ASTM D3039
Compressive strength (transverse direction), σ_{2c}	141 MPa	ASTM D6641

In-plane shear strength, τ_{12}	100 MPa	Tomblin [9]
Cohesive bond normal stiffness, K_{nn}	5000 GPa/mm	Turon, et al, [12]
Cohesive bond shear stiffness, K_{ss}	2500 GPa/mm	Turon, et al, [12]
Cohesive bond normal strength, S_n	35 MPa	ASTM D5528
Cohesive bond shear strength, S_s	90 MPa	JIS K7086-1993
Mode I fracture toughness, G_{IC}	0.258 mJ/mm ²	ASTM D5528
Mode II fracture toughness, G_{IIC}	0.723 mJ/mm ²	JIS K7086-1993
Mixed-mode loading parameter, η	1.75	Camanho and Dávila, [14]

3 Experimental and simulation results

Numerical simulations without accounting for failure were also carried out. Only the elastic properties in Table 4 were used in the simulations. These simulations were 10 to 15 times faster than those with failure and provided useful information on when the accumulated damage in the specimens starts to cause observable deviation in the load-displacement plots compared to the situation of zero damage as shown in Figure 3.

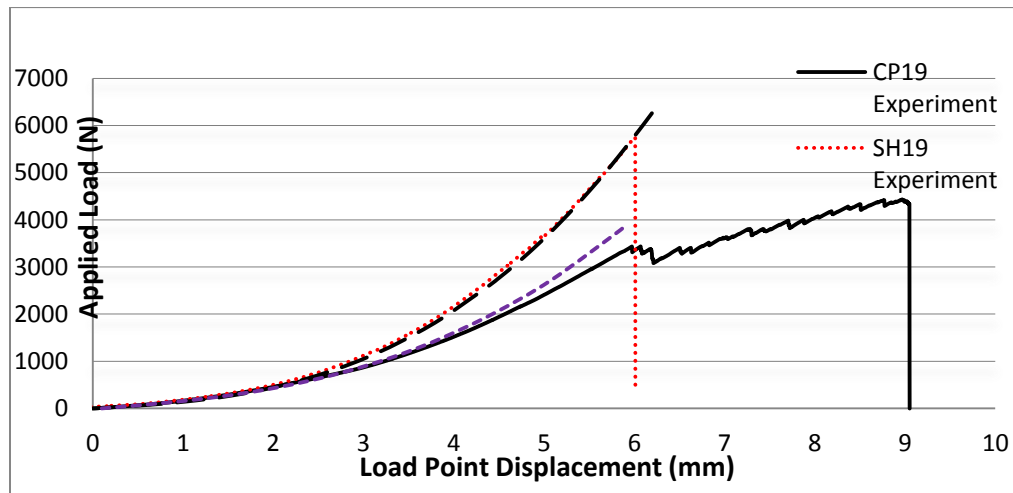


Figure 3. Load vs displacement curve of SH19 and CP19 under computations without accounting for damage (simulation) and actual experiment

It is seen that SH19 specimens are always stiffer than CP19 specimens. Interestingly, the load bearing capability of SH19 seems to be insensitive to damage until catastrophic failure at 6.5mm displacement. It is noted that audible cracking sounds were detected in SH19 specimens as early as 4.5mm displacement and some delamination was observed under the microscope at this point. Both experiments and simulations without damage gave almost identical load-displacement response up till the point of catastrophic failure. In contrast, the actual load-displacement plots of CP19 specimens begin to deviate from the simulations without damage at a displacement of about 4mm although the first load drop occurs at 6.5mm.

3.1 Damage evolution in SH19

It is found from the simulations that at the early stage of the transverse loading (at about 3mm displacement), cohesive layer 9, located at the mid-plane, experiences the highest shear stress, which causes delamination to initiate. The delamination continues to grow until final failure, creating a large

delamination. CT-scan of the specimens also showed one large delamination near mid-plane of the laminate.

Simulations also indicated element of the plies on either side of cohesive layer 9, i.e., plies 9 and 10, experience sudden tensile and compressive stresses along fiber direction when delamination occurs locally. When delamination reaches a local element, it will experience compression in ply 9 and tension in ply 10. This means the large delamination area affects stresses which in turn affect the damage patterns of SH19.

Based on the simulations and CT-scans, load drop appears at the instance when the crack front of matrix splitting and fiber damage merge with the large delamination in the middle plane. *Figure 4* shows part of images from CT-scans together with corresponding plots depicting damage predicted by simulations at final damage stage of SH19.

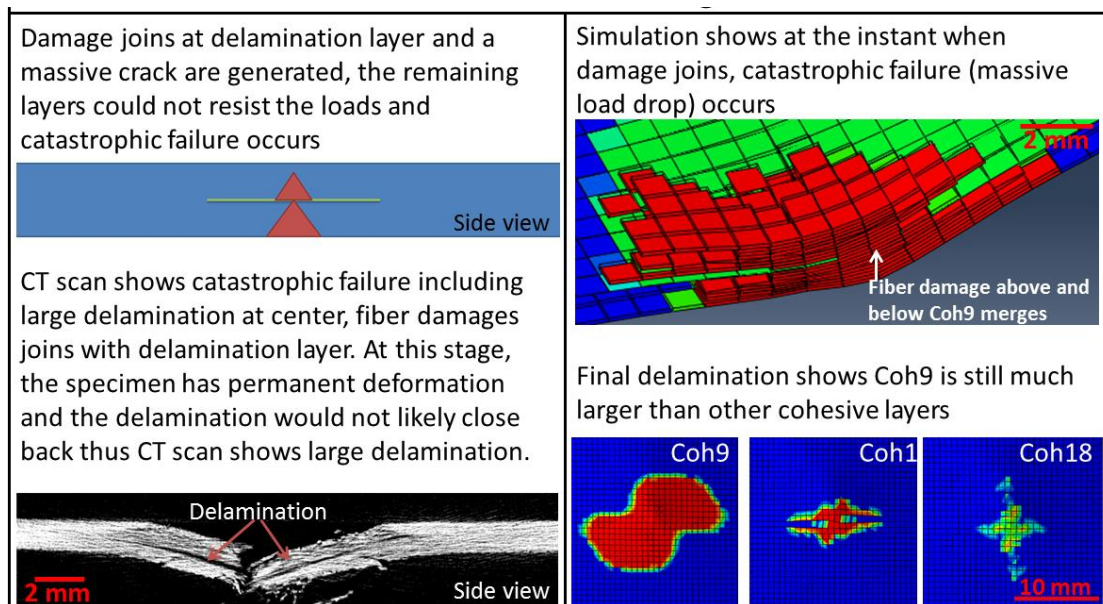


Figure 4. combined observation of CT scan and simulation of SH19, for the picture on the upper right side of this figure, the green elements represents delamination of Coh9, the red elements represents fiber damage; for the picture on the lower right side of this figure, red elements represents delamination, where green elements represents elements the verge of delamination

3.2 Damage evolution in CP19

Both simulation and CT-scans of specimens showed that CP19 experiences delamination at multiple inter-ply interfaces at 4.5mm indenter displacement. Fiber damage and matrix splitting begin from the bottom layers and grow towards the top layers. Load drops appear whenever the crack front meets with a delaminated interface, lowering the stiffness of the plate upon each load drop. *Figures 5* shows part of CT-scan images of the specimens and their corresponding simulation predictions.

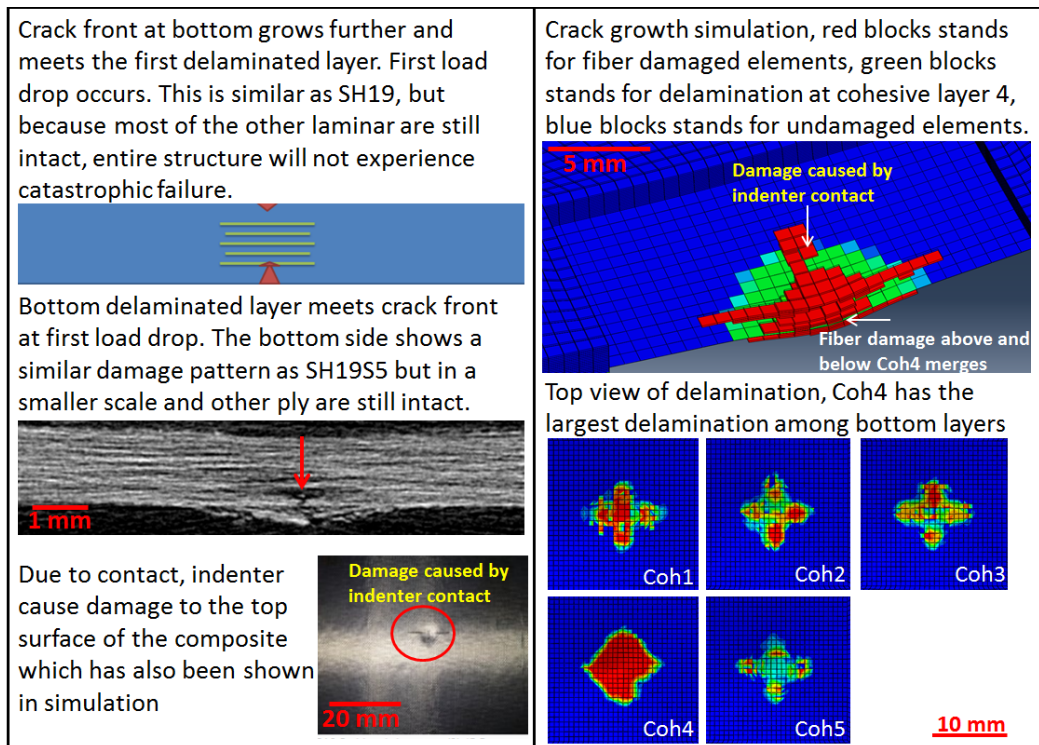


Figure 5. combined observation of CT scan and simulation of CP19 on the first load drop

4 Conclusions

The merging of the fiber/matrix damage and the large delamination causes the catastrophic load drops for transverse loadings. The delamination can be controlled by changing the orientations between each ply to alter its stiffness pattern. For SH19, a single large delamination occurs at or close to the mid-plane of the laminate where CP19 has multiple delaminations.

SH19 outperforms CP19 because SH19 has high stiffness; the fiber/matrix damage initiating from the bottom surface in SH19 has to grow further to reach the delamination layer located at middle and will not cause load drop until final failure. This allows a large increase in stiffness and maximum load bearing capability.

References

- [1] Y. Bouligand, Sur une architecture torsadée répandue dans de nombreuses cuticules d'Arthropodes, CR Acad. Sci. Paris 261 (1965) 3665e3668.
- [2] J. S. Shang, N. H. H. Ngern, and V. B. C. Tan, "Crustacean-inspired helicoidal laminates," Compos. Sci. Technol., vol. 128, pp. 222–232, 2016.
- [3] T. Apichattrabrut, K. Ravi-Chandar, Helicoidal composites, Mech. Adv. Mater. Struct. 13 (1) (2006) 61—76.
- [4] L. Cheng, A. Thomas, J.L. Glancey, A.M. Karlsson, Mechanical behavior of bioinspired laminated composites, Compos. Part A Appl. Sci. Manuf. 42 (2) (2011) 211e220.

- [5] S. Hong, D. Liu, "On the relationship between impact energy and delamination area." *Experimental mechanics* 29.2 (1989): 115-120.
- [6] J. Andersons, M. König, Dependence of fracture toughness of composite laminates on interface ply orientations and delamination growth direction, *Compos. Sci. Technol.* 64 (13) (2004) 2139e2152.
- [7] K. Ravi-Chandar, *Design optimization and characterization of helicoidal composites with enhanced impact resistance*. TEXAS UNIV AT AUSTIN CENTER FOR MECHANICS OF SOLIDS STRUCTURES AND MATERIALS, 2011.
- [8] B. Chen, D.G. Yin, Q. Yuan, J. Luo, J.H. Fan, "Model and Maximal Pull-out Force of Helicoidal Fiber Structure in the Underpinnings of Tumblebug Cuticle." *Materials Science Forum*. Vol. 686. Trans Tech Publications, 2011.
- [9] J. Tomblin, J. Sherraden, W. Seneviratne, K.S. Raju, "Advanced General Aviation Transport Experiments. A–Basis and B–Basis Design Allowables for Epoxy–Based Prepreg Toray T700GC-12K-31E/# 2510 Unidirectional Tape." National Institute for Aviation Research Wichita State University, Wichita, Kansas (2002).
- [10] M.H. Dato, *Mechanics of fibrous composites*. Springer Science & Business Media, 2012. 333—365.
- [11] M.W. Hyer, *Stress analysis of fiber-reinforced composite materials*. DEStech Publications, Inc, 2009. 236-270
- [12] A. Turon, C.G Davila, P.P Camanho, J. Costa, "An engineering solution for mesh size effects in the simulation of delamination using cohesive zone models." *Engineering fracture mechanics* 74.10 (2007): 1665-1682.
- [13] S.W. Tsai, E.M. Wu, "A general theory of strength for anisotropic materials." *Journal of composite materials* 5.1 (1971): 58-80.
- [14] P.P. Camanho, C.G. Dávila, "Mixed-mode decohesion finite elements for the simulation of delamination in composite materials." (2002) 33.
- [15] S.T. Pinho, P. Robinson, L. Iannucci. "Fracture toughness of the tensile and compressive fibre failure modes in laminated composites." *Composites science and technology* 66.13 (2006): 2069-2079
- [16] BW Kim, AH Mayer. "Influence of fiber direction and mixed-mode ratio on delamination fracture toughness of carbon/epoxy laminates." *Composites Science and Technology* 63.5 (2003): 695-713.
- [17] T.A. Sebaey, et al. "Damage resistance and damage tolerance of dispersed CFRP laminates: Effect of the mismatch angle between plies." *Composite Structures* 101 (2013): 255-264.
- [18] D. Liu. "Impact-induced delamination—a view of bending stiffness mismatching." *Journal of composite materials* 22.7 (1988): 674-692.